Materials Science & Engineering A 909 (2024) 146821

Contents lists available at ScienceDirect

Materials Science & Engineering A

journal homepage: www.elsevier.com/locate/msea

Effect of surface topography on the fatigue behavior of additively manufactured Ti6Al4V and CoCr alloys

Amanda Heimbrook [a,*], Ken Gall [a,b]

[a] Department of Mechanical Engineering and Materials Science, Duke University, Durham, NC, 27708, USA
[b] Restor3d, 4001 NC-54 #3160, Durham, NC, 27709, USA

ARTICLE INFO

Keywords:
Fatigue
CoCr
Ti6Al4V
Powder bed fusion
Post-processing

ABSTRACT

Powder bed fusion (PBF), including selective laser melting and electron beam melting, fabricates complex, porous, osseointegrative implants for widespread clinical use. Fatigue testing is imperative for predicting long-term strength and durability of rough and surface porous implants while bone remodels around and grows into the implant. This study analyzes different materials (Ti6Al4V and Co28Cr6Mo) with varying topographies including as-printed surface roughness and the addition of a surface porous layer common to implants. The results are compared to wrought and PBF controls that are polished and machined. Moreover, different PBF techniques for titanium result in different as-printed surface roughness (~0.07–17 μm) and microstructure. The fatigue data demonstrates that the surface finish impact was stronger in Ti6Al4V versus CoCr and SLM Ti6Al4V HIP + surface porous gyroid samples didn't perform worse than the roughest solid sample without surface porosity (EBM Ti6Al4V). With the same mechanical surface finishes, the SLM and wrought Ti6Al4V samples display similar fatigue resistance (800 and 850 MPa respectively), while EBM samples remain inferior (350 MPa). This study provides a foundation to compare fatigue resistance across materials and surface topographies through different fabrication techniques to optimize the lifespan of orthopedic implants while incorporating rough as printed surfaces and added surface porosity, both of which are essential for osseointegration.

1. Introduction

Additive manufacturing (AM), specifically powder bed fusion (PBF), has grown in popularity across multiple fields including the biomedical field for metallic orthopedic implants [1]. This process excels in producing customizable, precise, and complex metal lattices (such as the triply periodic minimal surface (TPMS) gyroid). These lattices, specifically the gyroid, are beneficial for promoting osseointegration in part due to the superior mechanical properties compared to strut-based lattices [2]. In contrast, subtractive manufacturing, such as machining, remains a useful technique for solid implants where patient specificity, porosity and surface roughness are not needed such as in standardized bone plates. While there are tradeoffs to consider with both 3D printing and machining, depending on the application, subtractive manufacturing can also be implemented with PBF to leverage the strengths of both processes for certain device geometries [3].

In orthopedic implants that undergo repetitive and complex loading modes, defects (i.e., porosity or surface roughness that behave as micro notches) are inherent stress concentrations that act as crack initiation sites for fatigue failure [4]. Therefore, cyclic fatigue testing is imperative to predict the durability of implants over time. Other factors affecting fatigue life include cyclic stresses, residual stresses (from additive manufacturing techniques), material properties (strength and toughness), internal defects, microstructure, surface quality, surface porosity, oxidation, corrosion, etc. [5–7]. For high cycle fatigue (typically 100,000+ cycles), many cracks initiate at the surface defects, whereas in very high cycle fatigue (typically 10 million + cycles) the cracks tend to initiate at internal defects [8]. Research has been conducted on the factors contributing to surface finish and minimizing internal defects such as choice of material, type of manufacturing, optimizing manufacturing process parameters, thermal post-processing for material internal structure, and mechanical post-processing material external finish (machining, polishing, blasting) [9–13]. However, especially when comparing across studies, past research efforts typically do not

Abbreviations: AM, additive manufacturing; PBF, powder bed fusion; TPMS, triply periodic minimal surface; HIP, hot isostatic pressing; SLM, selective laser melting; EBM, electron beam melting.

* Corresponding author.
E-mail address: Amanda.heimbrook@duke.edu (A. Heimbrook).

https://doi.org/10.1016/j.msea.2024.146821
Received 4 January 2024; Received in revised form 29 February 2024; Accepted 11 June 2024
Available online 13 June 2024
0921-5093/

Table 1
Summary Table for various properties of the tested samples.

Sample Name	Post-processing	Microstructure	Surface Area Roughness (Sa)	Fatigue Strength
SLM Ti6Al4V HIP	HIP 1650 °F ± 25 °F @ 14,750 psi +250/-246 for 2 h	elongated α in a lamellar α+β dual phase; Widmanstätten morphology	8.114 μm	325 MPa
SLM Ti6Al4V HIP + blasted	HIP 1650 °F ± 25 °F @ 14,750 psi +250/-246 for 2 h + blasted		5.141 μm	375 MPa
SLM Ti6Al4V HIP + machined	HIP 1650 °F ± 25 °F @ 14,750 psi +250/-246 for 2 h + machined		0.203 μm	875 MPa
SLM Ti6Al4V HIP + polished	HIP 1650 °F ± 25 °F @ 14,750 psi +250/-246 for 2 h + polished		0.070 μm	800 MPa
EBM Ti6Al4V	As built	Fine lamellar α+β dual phase; basket weave morphology	17.24 μm	175 MPa
EBM Ti6Al4V + polished	As built + polished		0.109 μm	350 MPa
wrought Ti6Al4V + machined	Annealed @ 1300 °F for 2 h + machined	equiaxed α with dual phase lamellar α + β (transformed in between β)	0.238 μm	850 MPa
wrought Ti6Al4V + machined + polished	Annealed @ 1300 °F for 2 h + machined + polished		0.081 μm	850 MPa
SLM Co28Cr6Mo	Stress relief heat treated 1925 °F ± 25 °F for 2 h	precipitates formed at grain boundary and within the grains, predominantly γ	5.252 μm	375 MPa
SLM Co28Cr6Mo + machined	Stress relief heat treated @ 1925 °F ± 25 °F for 2 h + machined		0.197 μm	600 MPa
SLM Co28Cr6Mo + polished	Stress relief heat treated @ 1925 °F ± 25 °F for 2 h + polished		0.191 μm	525 MPa
SLM Ti6Al4V HIP + 0.25 mm gyroid	HIP 1650 °F ± 25 °F @ 14,750 psi +250/-246 for 2 h		N/A	200 MPa
SLM Ti6Al4V HIP + 0.5 mm gyroid	HIP 1650 °F ± 25 °F @ 14,750 psi +250/-246 for 2 h		N/A	150 MPa
SLM Ti6Al4V HIP + 0.75 mm gyroid	HIP 1650 °F ± 25 °F @ 14,750 psi +250/-246 for 2 h		N/A	175 MPa

employ the same fatigue testing controls, samples, or methods across all key permutations of the critical surface and processing variables. In particular, the addition of surface porosity compared to the as printed rough surface has not been systematically analyzed in light of both printed and wrought, machined and polished controls.

Common metals implemented in orthopedic implants include Ti6Al4V and CoCr (specifically Co28Cr6Mo) due to their biocompatibility, corrosion resistance, and superior mechanical properties [1,14,15]. In PBF, these metals can be melted either through a laser source (Selective Laser Melting, SLM) or an electron source (Electron Beam Melting, EBM) [16,17]. Different processing parameters alter the energy density and will impact the quality of the manufactured part [18,19]. Moreover, when the molten metal cools in PBF, surrounding powder will adhere, which adds to the inherent surface roughness of a sample and lowers the fatigue properties in the as-built surface finish condition [20,21]. While most mechanical properties are lowered due to a rough as-printed surface, the roughness enhances osseointegration leading to an inherent tradeoff in the impact of surface roughness and porosity [22]. The wrought Ti6Al4V counterparts (made by deformation processing and shaping the material in the solid state and then heat treating it) are almost always machined down to their final shape, so there is less inherent surface roughness compared to as-built PBF surfaces.

3D printed and wrought manufactured parts often receive thermal post-processing to minimize defects and favorably alter the microstructure of the material. Thermal post-processing can include stress relief, heat treatment and hot isostatic pressing (HIP) all of which can alter the final microstructure and therefore mechanical properties [23]. HIP applies high temperatures and pressure to decrease the internal voids caused by processing and will in turn increase the mechanical strength and fatigue life [24,25]. In one study, SLM CoCr as built samples had a fatigue strength of 135 MPa at 2 million cycles, which increased to 319 MPa with HIP, and further improved to 380 MPa with heat treatment, with all variations displaying changes in microstructure and ratio of phases [26]. Moreover, the SLM process can produce residual stresses from the temperature gradients due to fast cooling rates. Thermal treatments are common for SLM parts as they help minimize residual stress and therefore improve resistance to crack initiation [27]. EBM, on the other hand, requires a preheated temperature (which acts as an in-process heat treatment), and has less of a temperature gradient during cooling resulting in less stress buildup and warping for the as-printed parts [6]. When comparing fatigue strength amongst PBF processes, Vayssette et al., concluded that both SLM Ti6Al4V HIP and EBM HIP Ti6Al4V parts display a lamellar microstructure, yet, the roughness of the EBM parts caused a twofold decrease of fatigue stress at runout (222.5 MPa for SLM HIP and ~111.2 MPa for EBM HIP at 2 million cycles in fully reversed loading) [28].

Surface post-processing alters material external finish by eliminating surface defects with machining, polishing, or powder blasting but cannot be practically applied to complex lattice PBF parts. These surface post-processing techniques can be done individually or in addition to thermal post-processing. Compared to Ti6Al4V samples with rough as-built surfaces, machined samples typically have fatigue cracks initiating from either surface discontinuities or internal defects, whereas as-built samples with rough surfaces almost always experience crack initiation at the samples surface [29]. Moreover, machining (removing surface roughness) improves fatigue life, and machining on top of HIP further increased the fatigue strength [29,30]. Polishing can also minimize cyclic stressors (i.e., minimize stress concentrations to enhance fatigue) with processes such as mechanical polishing, chemical polishing, electro polishing, laser polishing, or a combination of the sorts [31–35]. After mechanically polishing a SLM part's surface, there can be improved monotonic tensile strength and fatigue strength due lower roughness and compressive residual stress induced at the surface [36]. For SLM Ti6Al4V samples in tested in tensile fatigue by Jamshidi et al., the as-printed samples had a fatigue strength of ~50 MPa at 10 million cycles, but increased to ~200 MPa after HIP, and further increased to ~300 MPa with HIP and wet polishing [37].

Although research on individual factors influencing fatigue has been published, there is a need to systematically compare multiple surface topographies under identical testing conditions and using an appropriate fatigue sample geometry. It is widely known that increased surface roughness lowers fatigue strength, yet there is little to no

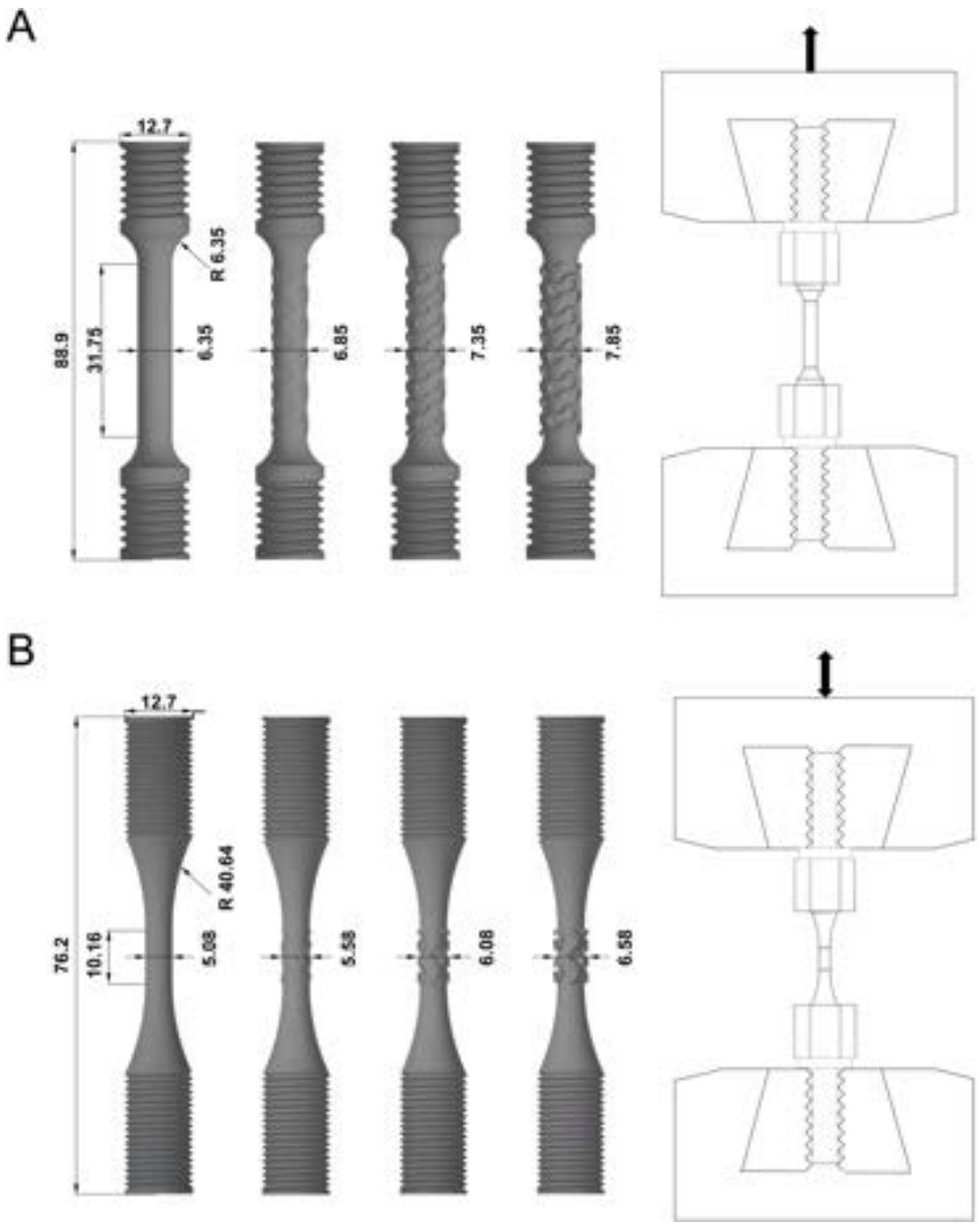

Fig. 1. Test set up of A) representative tensile samples after post-processing and with different surface porous gyroid samples (measurements in mm) and tensile test set up B) representative high cycle fatigue samples after post-processing and with different surface porous gyroid samples (measurements in mm) as well as HCF test set up.

information on how the deliberate addition of surface porosity impacts fatigue strength relative to as printed roughness and smooth wrought and 3D printed controls. The current study encompasses testing different materials (Ti6Al4V and Co28Cr6Mo), various manufacturing techniques (wrought, 3D printed by SLM, and 3D printed by EBM), and different surface finishes (porous, as-printed, blasted, machined, and polished) to better understand the influence of these variables on both monotonic mechanical properties and fatigue behavior. The cylindrical dogbones tested under stress-controlled tensile high cycle fatigue (HCF) include the following solid sample groups: SLM Ti6Al4V HIP (as-printed surface, blasted surface, machined surface, polished surface); EBM Ti6Al4V (as-printed surface and polished surface) wrought Ti6Al4V (machined surface, machined + polished surface); SLM Co28Cr6Mo (as-printed surface, machined surface, and polished surface). Additionally, this study establishes how the intentional addition of surface porosity (0.25 mm, 0.50 mm, 0.75 mm layer thickness of 65 % porous gyroid onto the surface of the solid SLM TI6Al4V HIP parts) impacts the fatigue strength. The gyroid is analyzed as it allows for bone to grow in, however the addition of the lattice introduces intentional defects where stress can concentrate and lower the mechanical properties compared to the solid counterpart. Ultimately, this work provides a foundational and systematic study of the impact of multiple surface topographies on fatigue properties of 3D printed metals (using common process and post processing techniques documented in literature) relative to wrought Titanium material counterparts. The fatigue data is one essential component in understanding how to design and alter the surface of 3D printed implants to maintain fatigue resistance while still offering opportunity for enhanced osseointegration.

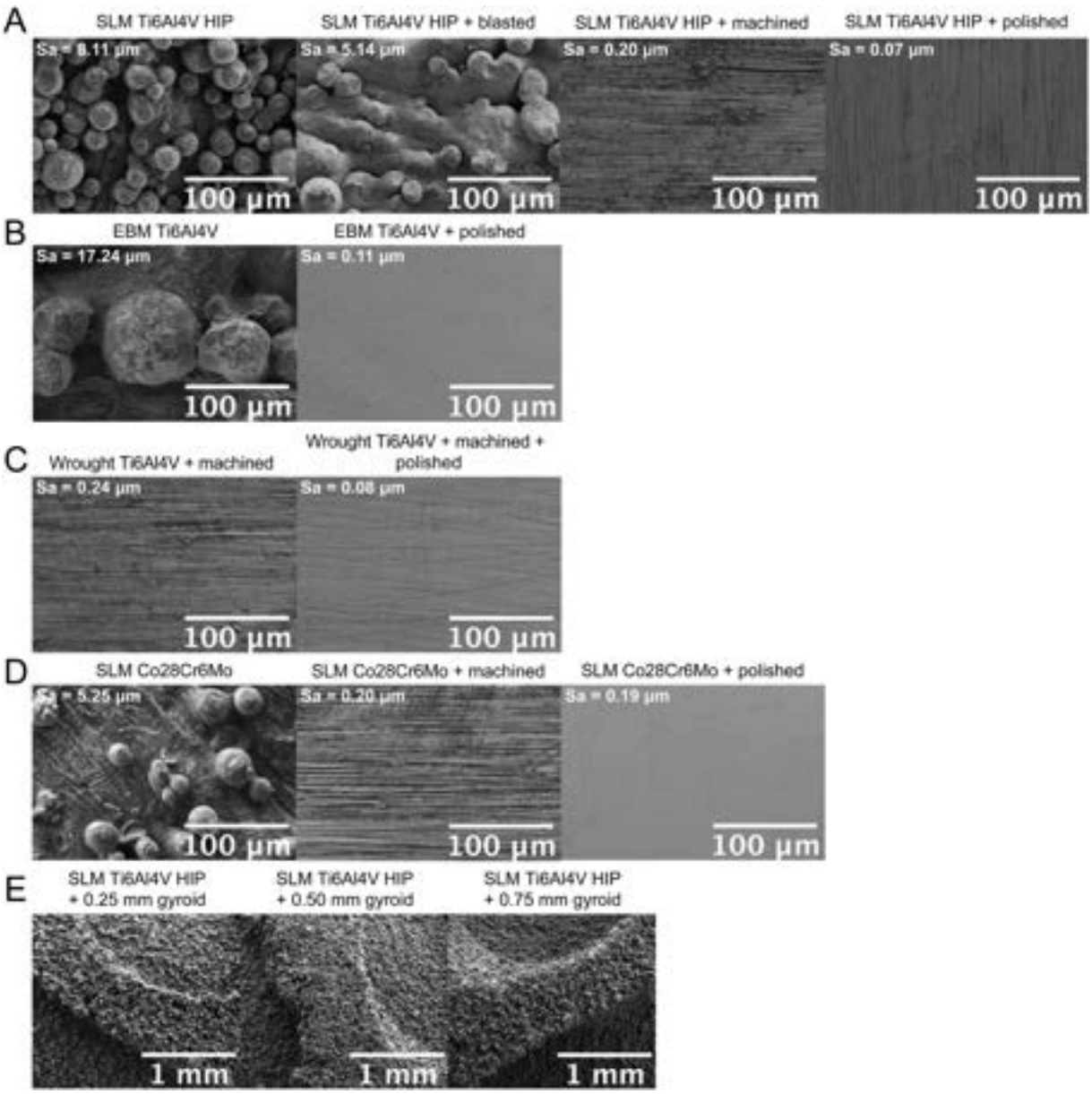

Fig. 2. SEM images and roughness measurements (rounded to the hundredths) of the surface of A) SLM Ti6Al4V HIP variations B) EBM Ti6Al4V variations C) wrought Ti6Al4V variations D) SLM Co28Cr6Mo variations E) SLM Ti6AlV HIP + gyroid.

2. Material and methods

2.1. Manufacturing and thermal post-processing

An overview of the sample names, manufacturing and post-processing methods can be found in Table 1. All 3D printed parts were designed in Solidworks. For both tensile and fatigue samples there were two variations: a dogbone with round ends and a cylindrical bar that would be machined down to a dogbone (Fig. 1). For the SLM Ti6Al4V parts, 0.25 mm, 0.50 mm, and 0.75 mm of gyroid was added to the surface of the designed dogbone part during printing (Fig. 1). The gyroid had a 6x6x6 unit cell size and 0.75 mm wall thickness and was applied using 3DXpert. Parts were printed within a validated section of the build plate in the same direction of loading (tensile).

The SLM Ti6Al4V samples and SLM Ti6Al4V gyroid parts were printed in an inert Argon atmosphere (3D Systems, DMP ProX 320; DMP ProX 350 for blasted samples) using grade 23 ELI Ti6Al4V feedstock powder 15–45 µm particle size distribution (AP&C) and default laser parameters (part LT30 in 3DXpert). For the gyroid lattice, refined infill parameters were used (145 W laser power, 1000 mm/s scanning speed, and 50 µm laser focus) [38].

All SLM Ti6Al4V parts (including surface gyroid parts) underwent hot isostatic pressing (HIP) at 1650 °F ± 25 °F at 14,750 psi +250/-246 for 2 h in accordance with ASTM 2924 -14. The samples were removed from the build plate via wire electronic discharge machining (EDM).

The Co28Cr6Mo samples were printed in an inert Argon atmosphere using a 3D Systems DMP ProX 350 system with 3DSystems CoCr F75 powder (15–53 µm particle size). Laser parameters of 250 W laser power and 1000 mm/s scanning speed were used for a single contour scan and infill. All SLM Co28CrMo parts underwent stress relief annealing at 1925 ± 25 °F for 2 h. The samples were removed from the build plate with a wire EDM.

The EBM Ti6Al4V samples were printed using a Arcam Q10plus V2.1 machine with Ti–6Al–4V feedstock powder (45–146 µm particle size distribution). The layer thickness was 50 µm, acceleration voltage was 60 kV and max beam current varied throughout the process but had a

maximum of 50 mA. No further heat treatment was used. After printing, samples were mechanically removed from the plate during cooling with no additional tools required.

The wrought Ti6Al4V (deformation processed and annealed) samples were Grade 5 bars in accordance with ASTM B348 from Titanium Processing Center. The annealing took place at 1300 °F for 2 h. The stock bars for tensile samples were 15.875 mm diameter and 78.74 mm long and the stock fatigue samples were 15.875 mm in diameter and 88.9 mm long.

2.2. Mechanical surface post-processing

All samples were threaded tensile or fatigue dogbones in accordance with ASTM E8 and ASTM E466. The cylindrical wrought, SLM Ti6Al4V, and SLM CoCr samples were machined down to a dogbone shape with threaded ends. A set of samples from the SLM Ti6Al4V HIP, SLM Co28Cr6Mo, EBM Ti6Al4V, and Wrought Ti6Al4V were polished from the as built dogbone shape using increasingly fine grit paper in a process standard in the polishing of total joints for articulation. Polishing by hand occurred until the desired mirror finish was reached. The wrought Ti6Al4V samples were the only samples that received machining before polishing. A group of SLM Ti6Al4V HIP samples were blasted with Ti6Al4V particles ranging from 15 to 45 μm.

2.3. Surface SEM images

All SEM images were captured using an Apreo S by ThermoFisher Scientific (formerly FEI) using a voltage of 2.00 kV and current of 25 pA. Images shown are using the Everhart – Thronley Detector (EDS) using secondary electrons at a working distance of around 7 mm.

2.4. Roughness measurements

All roughness measurements were taken on a Filmetrics Profilometer Standard with a 100 mm × 100 mm stage under 10× Nikon DI objective lens with a zoom of 4x using white light interferometry. Three measurements were taken of different parts of the gauge section of the representative tensile sample.

2.5. Microstructure

Micrographs were prepared based on the cross-sectional area of the sample. Samples were cut by a water-cooled abrasive blade, then cleaned with ethanol and acetone and pressure mounted. From there, the sample was ground with silicon carbide abrasives and polished with a diamond suspension and fine polished with colloidal silica (ASTM E3).

Titanium samples were micro etched with Kroll's reagent and Co–Cr samples were etched with ASTM 20, per ASTM E 407.

Optical microscopes (Leica DMI500) captured the micrographs at 500x, per ASTM E 883.

2.6. Mechanical testing

Tensile and fatigue tests were based on ASTM E8 (tensile) and E466 (fatigue) samples and test protocols. All mechanical tests were on an MTS Landmark servo hydraulic test system. The samples were threaded into custom made jigs (hardened stainless steel). Tensile tests (n = 4) were performed at a rate of 1 mm/min and fatigue testing was performed at a frequency of 10 Hz and R = 0.1 with n = 2 at each stress level. Tensile fatigue tests at 10 Hz were chosen to represent the worst case scenario of loading. Sample runout was defined as n = 2 reaching 1 million cycles at a given stress level. The jig was held into vee notch grips at a pressure of 1250–1500 psi. The stress was calculated using the cross-sectional area of only the base solid region for each sample,

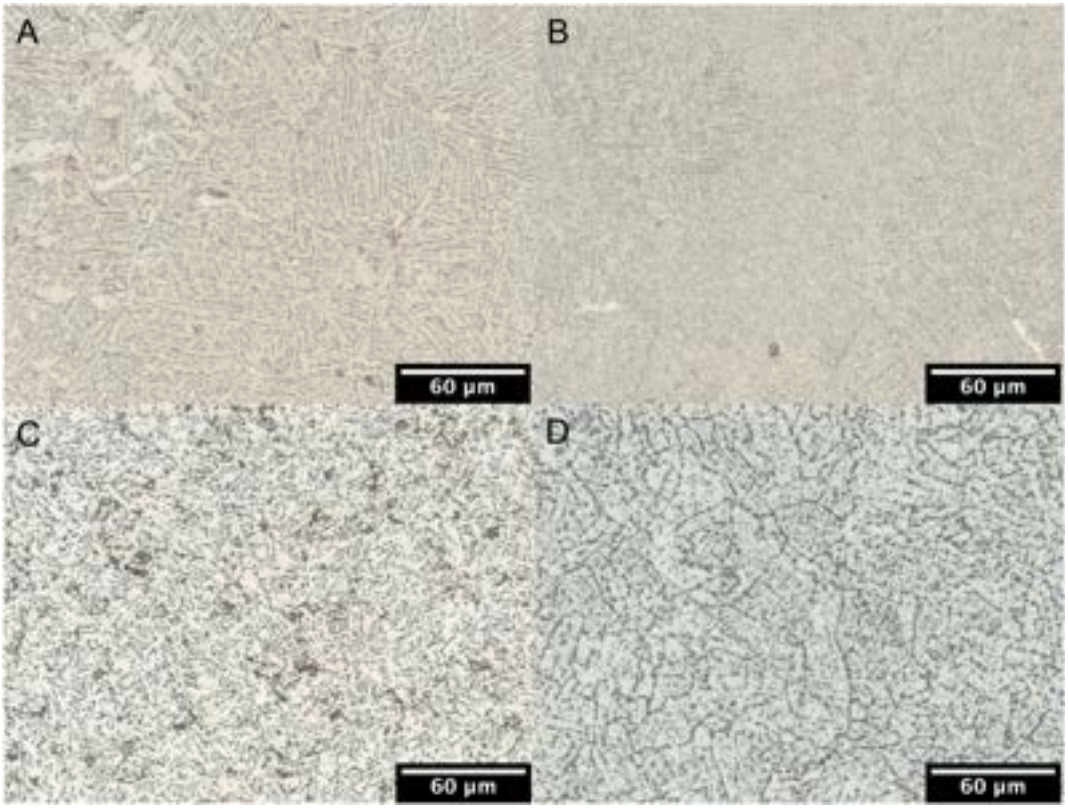

Fig. 3. Micrographs of a representative sample in the A) SLM Ti6Al4V HIP B) EBM Ti6Al4V as-printed C) wrought Ti6al4V and D) SLM Co28Cr6Mo manufacturing groups.

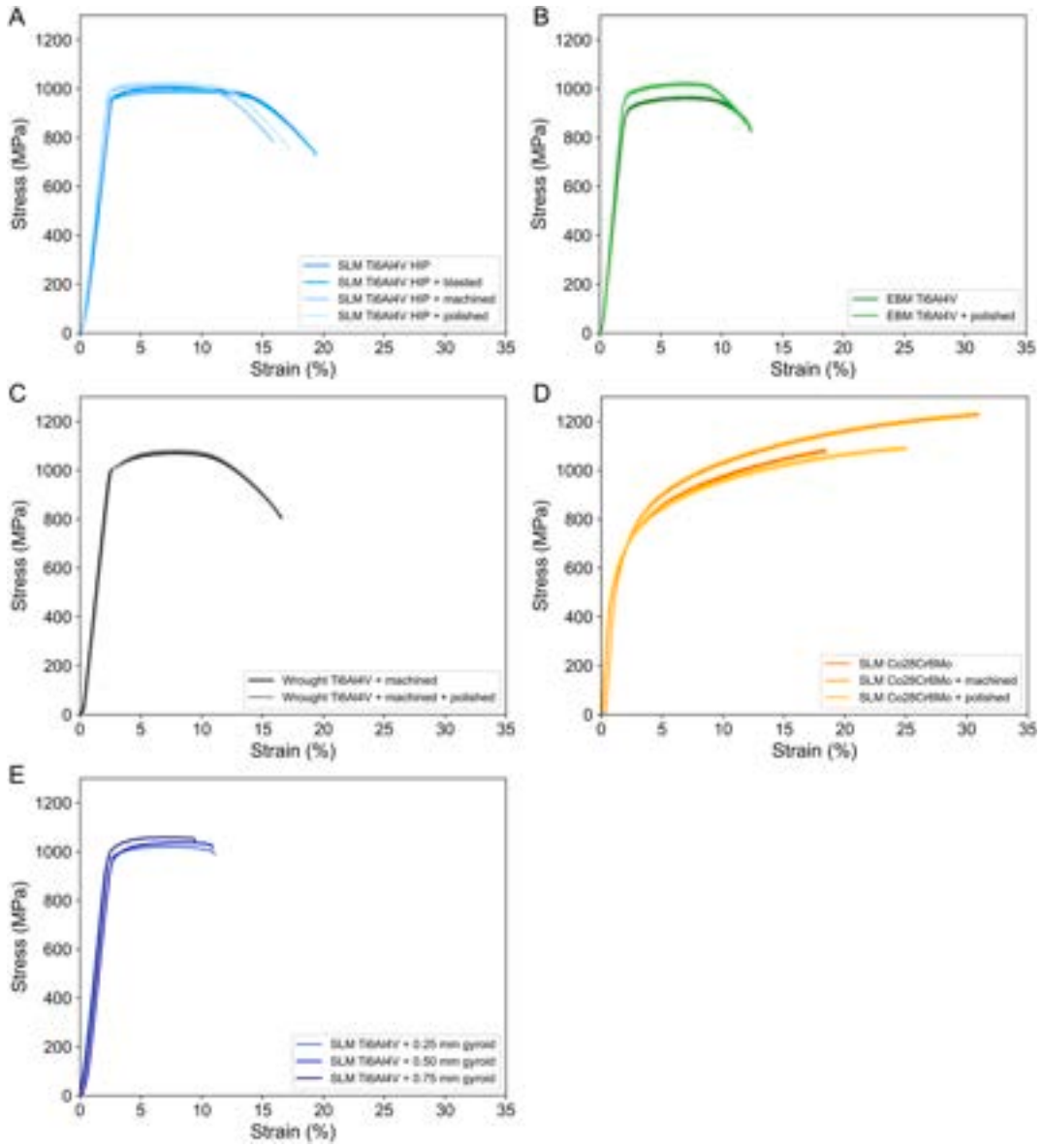

Fig. 4. Static tensile stress strain curves of A) SLM Ti6Al4V HIP variations B) EBM Ti6Al4V variations C) wrought Ti6Al4V variations D) SLM Co28Cr6Mo variations and E) SLM Ti6Al4V HIP + gyroid variations.

including the porous gyroid samples.

2.7. Fracture analysis

Optical images were obtained with an AM scope FMA050 with a LED-144. SEM images were taken using the same parameters as mentioned in *Surface SEM Images*.

3. Results and discussion

3.1. Surface analysis (roughness)

The average surface area roughness measurements (arithmetic mean height, Sa) are quantified in Table 1 and Supplementary Table 1 along with SEM images of the surfaces which can be found in Fig. 2. Within each sample group (i.e., SLM Ti6Al4V HIP, Wrought Ti6Al4V, EBM Ti6Al4V, and SLM Co28Cr6Mo), the mechanical post-processing greatly reduces the surface roughness of the sample.

The surface of pre-mechanical post-processed PBF parts (SLM Ti6Al4V HIP, EBM Ti6Al4V and SLM Co28Cr6Mo) display roughness from solidified melt pools as well as adhered unmelted particles. These are both characteristic of the PBF process due to the laser/electron beam path, melting/solidification, and thermal diffusion. The EBM Ti6Al4V samples have a larger particle size distribution (necessary for this fabrication method) compared to SLM Ti6Al4V HIP and thus appear to have larger solidified melt pools and larger particles adhered to the surface. The combination of the two factors doubles the surface roughness of the EBM Ti6Al4V parts compared to the SLM Ti6Al4V HIP parts (approximately 17 μm vs 8 μm). The SLM Co28Cr6Mo samples display fewer and smaller adhered unmelted particles compared to both EBM Ti6Al4V and SLM Ti6Al4V HIP samples, which decreased the roughness of the SLM Co28Cr6Mo sample to 5 μm. There are not as distinguishable solidified melt pools in the SLM Co28Cr6Mo samples which also contribute to the smoother surface.

The SLM Ti6Al4V HIP + blasted sample has far fewer adhered unmelted particles and this powder blasting processing revealed more of the solidified melt pools. Titanium powder blasting reduced the surface roughness to about 5 μm which is about two-thirds the roughness of the SLM Ti6Al4V HIP parts and approximately the same roughness as the SLM Co28Cr6Mo sample. Independent of the material and method of

manufacturing, machining the samples brought the roughness down to approximately 0.2 μm, ten times less than the lowest roughness as-printed surfaces. Machining lines are observed on the sample surface, which can be accounted for in the surface roughness. Polishing the surface further decreased the roughness to about 0.10 μm which is close to the standard for arthroplasty materials (about 50 nm). The SLM Ti6Al4V HIP + polished sample was the smoothest with a surface roughness of 0.07 μm (about 100 times smoother than the SLM Ti6AL4V part and a third of the roughness of the SLM Ti6Al4V + machined part). The EBM Ti6Al4V + polished sample had a surface roughness of ~0.11 μm (more than 150 times smoother than the EBM Ti6Al4V sample). The wrought Ti6Al4V + machined + polished samples were similar to the SLM Ti6Al4V HIP + polished sample with a roughness of 0.08 μm. The SLM Co28Cr6Mo sample was the roughest of the polished samples with a surface roughness of 0.19 μm.

The SLM Ti6Al4V HIP + gyroid samples displayed the same surface characteristics of the SLM Ti6Al4V HIP samples, with the gyroid section resulting in a purposely rough porous surface. While the porous surface structure could be a spot for stress to concentrate, the point for stress concentration will likely be where the gyroid wall edge meets the SLM Ti6Al4V HIP surface.

3.2. Microstructure

Representative micrographs presented in Fig. 3 illuminate the microstructure of each manufacturing group. Microstructure is consistent amongst samples in the same manufacturing group (i.e., SLM Ti6Al4V HIP, wrought Ti6Al4V, EBM Ti6Al4V, SLM Co28Cr6Mo) regardless of mechanical surface post-processing (i.e., Ti powder blasting, machining, polishing). For the Ti6Al4V samples, the light regions represent the α phase (Hexagonal close packed (HCP) crystal structure) and the dark regions represent the β phase (Body Centered Cubic (BCC) crystal structure) [39]. For the Co28Cr6Mo sample, the darkest regions represent the precipitates and the lighter gray represents the γ phase (Face Centered Cubic (FCC) crystal structure) [40].

The SLM Ti6Al4V HIP samples (Fig. 3A) have α at the prior β grain boundaries (called alpha grain boundaries which are a nucleation site) from which α colonies grew [41]. There are elongated α in an α+β dual phase and the α lamella show a Widmanstätten morphology (α lamella with intra-lamella β) [41,42]. Since these SLM Ti6Al4V parts received HIP as a post-processing treatment, any martensitic α′ formed from the fast cooling rates in the SLM would have decomposed into α+β during the post-processing [43]. Due to the higher processing temperature of EBM, there is an "in process" heat treatment for the decomposition of α′ into α+β, although some α' may still be present at the surface or where there are higher cooling rates [6]. The EBM Ti6Al4V samples (Fig. 3B) have α platelets that form at the α boundary as well as α at the prior β grain boundaries but is finer than the SLM Ti6Al4V HIP [44]. In the fine lamellar α+β dual phase (from the transformed β grains) needle like acicular α is present [21,45]. The arrangement of α lamella indicate a basket weave morphology (finer version of Widmanstätten) [44]. In many images of the EBM samples, there are microscopic circular defects indicating gas pores which will decrease the mechanical properties of the material [21]. The wrought Ti6Al4V samples (Fig. 3C) appear to have equiaxed α with dual phase lamellar α+β (transformed in between β) equiaxed alpha [21,46]. The α in the transformed β appears to be much finer (or acicular α). The SLM Co28Cr6Mo samples (Fig. 3D) depict well defined grain boundaries. Based on the phase diagram (not shown) there are precipitates such as carbides and intermetallic phases that can form at this temperature [39]. It appears that carbide precipitates grew along the grain boundaries and other precipitates formed within the grains [47,48]. Furthermore, the SLM Co28Cr6Mo appears to be predominantly γ FCC [40].

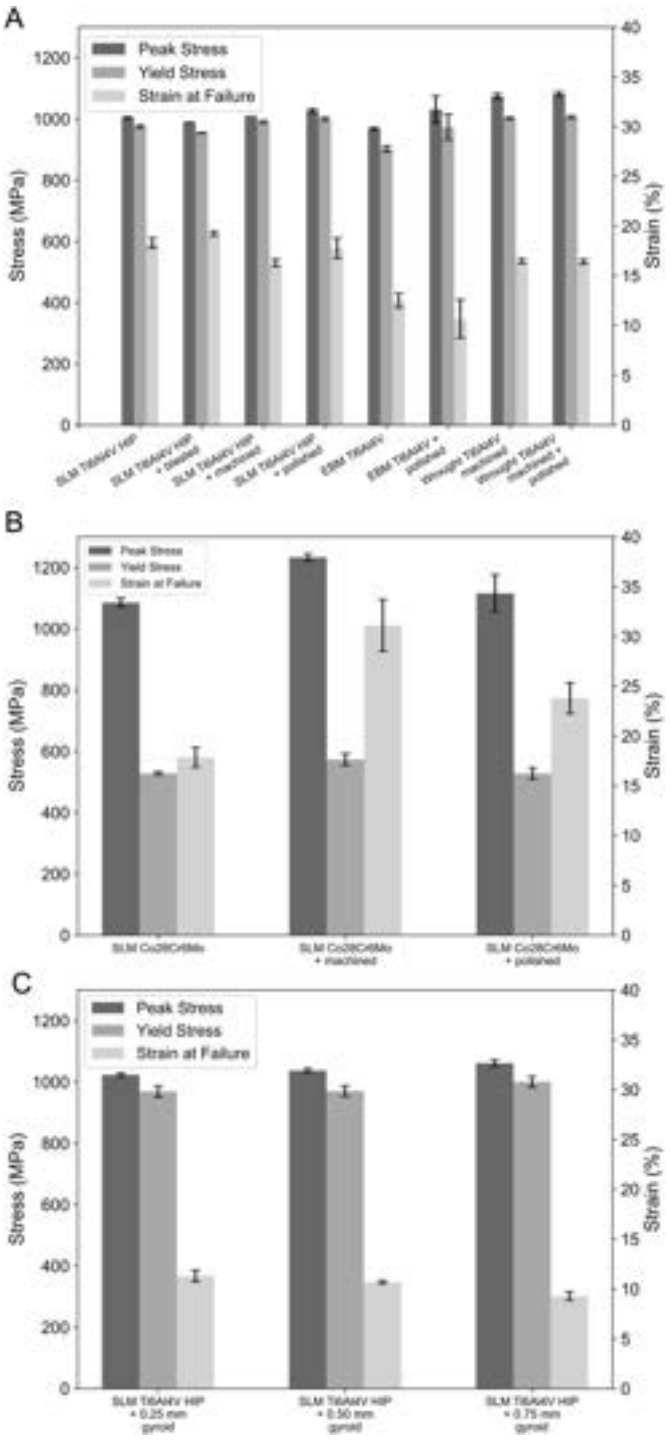

Fig. 5. Static tensile behavior of peak stress, yield stress, and strain at faiure for A) solid Ti6Al4V variations B) SLM Co28Cr6Mo variations and C) surface gyroid variations.

3.3. Tensile behavior

Stress strain curves from representative samples are depicted in Fig. 4 (all stress strain curves can be seen in Supplementary Fig. 1) and extracted tensile properties for all samples in each manufacturing group are displayed in Fig. 5, with error bars representing the standard deviation. All SLM Ti6Al4V and Co28Cr6Mo samples have a linear elastic region followed by a plastic region. The Ti6Al4V samples reach an ultimate tensile stress then stresses decrease until failure whereas SLM Co28Cr6Mo samples work harden until failure. The very rough and

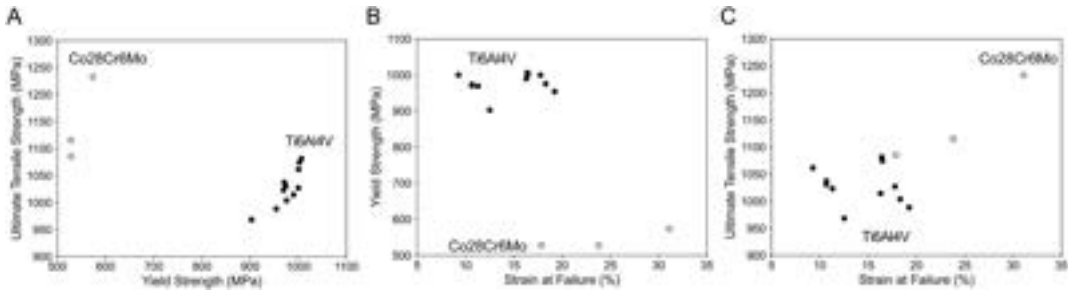

Fig. 6. Tensile behavior of A) ultimate tensile strength vs yield stress B) yield stress vs strain at failure C) ultimate tensile strength vs strain at failure.

surface porous SLM Ti6Al4V HIP + gyroid samples display a lower strain to failure compared to laser surface finishes (Fig. 4a) but comparable to the strain to failure of the rougher EBM Ti6Al4V samples (Fig. 4b).

Of the solid Ti6Al4V samples, mechanical post-processing of the samples generally increases the average peak stress and yield strength, but there isn't a distinct trend with strain at failure. While the wrought samples have the highest average peak stress and average yield strength, the SLM Ti6Al4V HIP and SLM Ti6Al4V HIP + blasted samples have the largest average strain at failure indicative of a metallurgical difference in the 3D printed and wrought samples given how rough the 3D printed samples are. EBM Ti6Al4V samples show lower strain to failure while the SLM Ti6Al4V samples show more ductility similar to the wrought samples.

Amongst the gyroid SLM Ti6Al4V HIP samples, average peak stress and yield stress increases, and the strain at failure decreases, with more added surface gyroid (from 0.25 mm to 0.75 mm gyroid). Overall, the average peak stress and yield stress of the gyroid samples is higher than the solid counterpart in SLM Ti6Al4V HIP, but the strain at failure is lower. This is due to the extra porous gyroid aiding in strength since the stress was calculated using the cross-sectional area of only the base solid region (i.e., 6.35 mm diameter instead of 6.85 mm, 7.35 mm or 7.85 mm diameters with the gyroid). However, the interface of the gyroid and solid acts as a stress concentration point causing lower strain to failure. These surface porous gyroid parts display a lower strain fracture closer to the EBM samples most likely due to the surface defects (roughness and porosity).

For the CoCr samples, the SLM Co28Cr6Mo + machined sample displayed the highest peak and yield stress as well as the highest strain at failure. Since machining and polishing refined the surface roughness, the strain at failure increased for a more ductile fracture.

There are some correlations between certain tensile mechanical properties (Fig. 6). When plotting ultimate tensile strength vs yield strength (Fig. 6A) and yield strength vs strain at failure (Fig. 6B), the Ti6Al4V and Co28Cr6Mo both display separate positive curved trends. For example, as yield increases so does the ultimate tensile stress. This remains true for the Co28Cr6Mo samples with regards to yield strength and strain at failure. However, the Ti6Al4V splits up into two separate trends based on process (Fig. 6B and C) when strength is plotted against strain to failure with the SLM Ti6Al4V HIP + gyroid and EBM Ti6Al4V samples being grouped together at lower strain to failure levels vs the SLM Ti6Al4V HIP and wrought Ti6Al4V samples grouped together at higher strain to failure levels. When the strain at failure increases, the yield strength and ultimate tensile strength tend to decrease for the Ti samples, but they do so at different rates for the SLM Ti6Al4V HIP + gyroid and EBM Ti6Al4V samples vs the SLM Ti6Al4V HIP and wrought Ti6Al4V samples. In both Fig. 6B and C, the SLM Co28Cr6Mo samples have a positive correlation compared to the Ti6Al4V samples. When plotting ultimate tensile strength vs strain at failure (Fig. 6C), the Ti6Al4V and Co28Cr6Mo overall become more cohesive which could indicate that for surface roughness treatments, as the ultimate tensile strength increases so does the strain at failure. Since strain at failure is indicative of ductility, having a strong sample that is also ductile can be a factor in determining fatigue life as local plasticity at notches and stress concentrations can impact the nucleation of fatigue cracks.

3.4. Fatigue behavior

Fatigue behavior between different materials (Ti6Al4V and Co28Cr6Mo), processes (wrought vs SLM and EBM), mechanical surface post-processing (powder blasted, machined, and polished) and added surface porous gyroid lattice (0.25 mm, 0.50 mm, and 0.75 mm) is overviewed in Fig. 7 and summarized in Table 1 (see Supplementary Table 2 for more data). For each sample group, two individual samples were tested at systematically decreasing levels of maximum applied

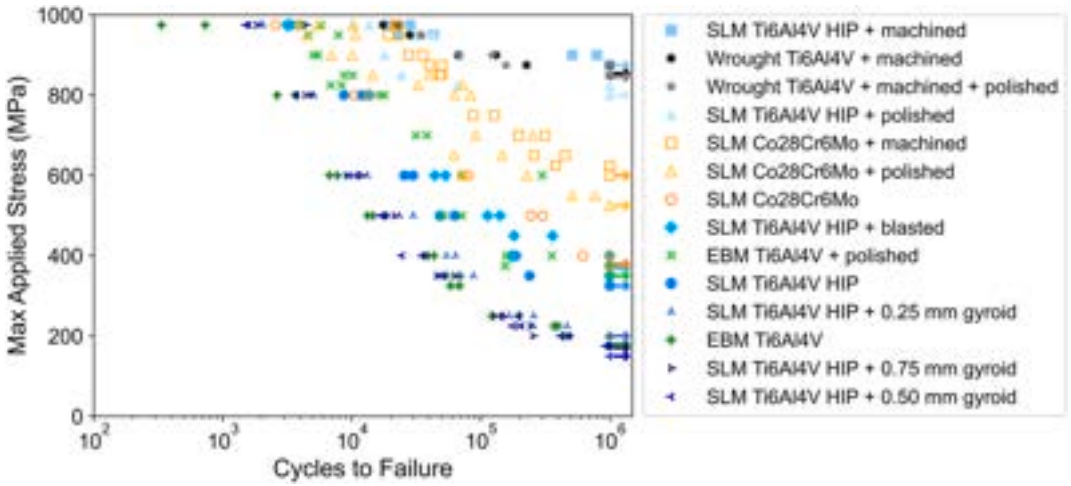

Fig. 7. Fatigue curves (maximum applied stress vs cycles to failure) of all sample variations.

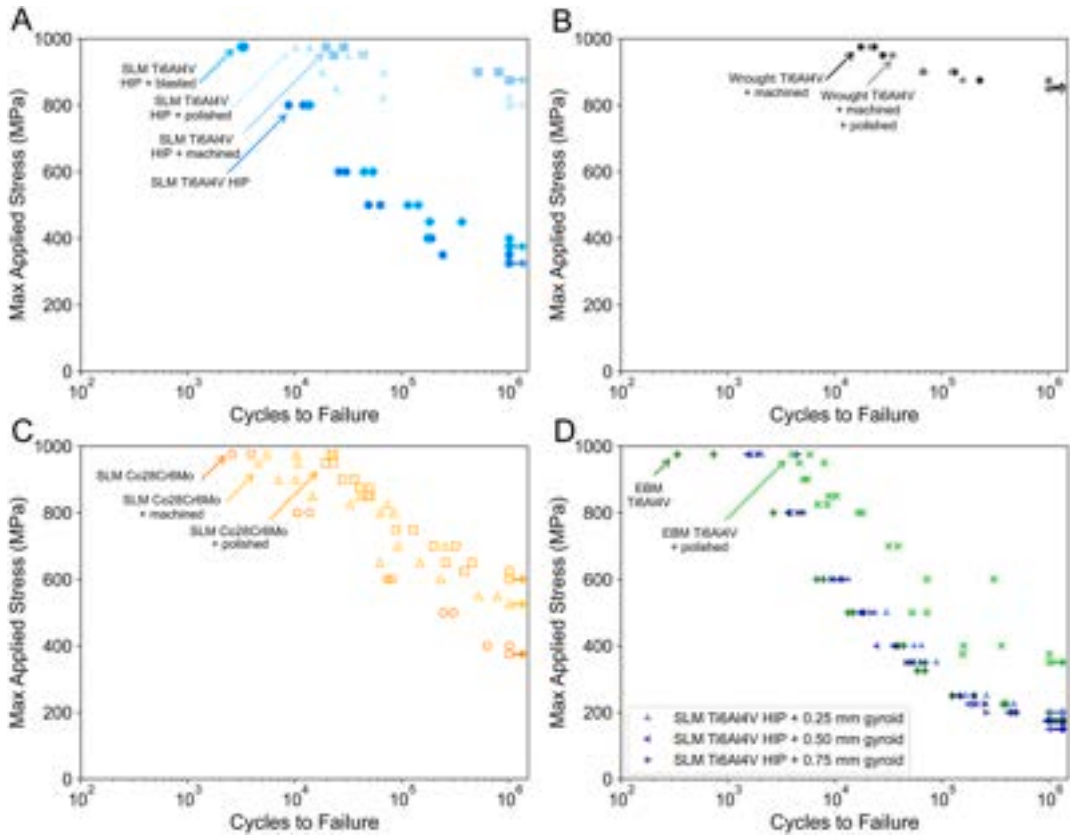

Fig. 8. Fatigue curves (maximum applied stress vs cycles to failure) of A) SLM Ti6Al4V HIP variations B) wrought Ti6Al4V variations and C) SLM Co28Cr6Mo variations and D) SLM Ti6Al4V HIP + gyroid variations.

stress until sample failure occurred, or runout hit one million cycles. The data in Fig. 7 will be separated and discussed based on the key sample variables for clarity.

3.4.1. *Surface finish effect*

The effect of surface finish on fatigue life is conveyed in Fig. 8 when each sample is grouped based on processing method and material (SLM Ti6Al4V HIP, Wrought TI6Al4V, EBM Ti6Al4V and SLM Co28Cr6Mo). The SLM Ti6Al4V HIP + surface gyroid samples were grouped with the roughest samples that were produced by EBM. In general, within the same process group (i.e., SLM Ti6Al4V HIP, Wrought Ti6Al4V, SLM Co28Cr6Mo, and EBM Ti6Al4V with SLM Ti6Al4V HIP + gyroid samples), the smoother the surface, the better the fatigue life of the sample. This can be explained by the surface roughness acting as micro notches on the surface for cracks to initiate due to the stress concentration. When the surface roughness increases, the size of the micro notches also increases and therefore less force is required for the cracks to initiate.

For the SLM Ti6Al4V HIP samples (Fig. 8A), machining the sample (decreasing surface roughness about 40x) increases the fatigue strength substantially from 325 MPa to 875 MPa, or almost 170 %, whereas polishing (decreasing the surface roughness by more than 100x) only increases the max applied stress at runout to 800 MPa, just less than 150 %. The polishing process is done by hand which can create macroscopic discontinuities (unevenness) within the gauge section of the fatigue sample (this does not occur in computer-controlled machining with a lathe) and therefore alters the stress concentrations and crack initiation points and is an imperfect polishing process. It is important to note that the machined samples were machined down from a solid cylinder shape whereas the polished sample was printed as a dogbone and polished directly, so there is a slight difference in the samples aside from just the surface finish that may be adding to lower fatigue strength in polished samples. However, compared to rougher alternatives, the properties of both machined and polished are similar to each other.

Blasting with Ti powder on the other hand (decreasing the surface roughness by ~36 %) only increases the fatigue life by 15 %. The slight increase can be attributed to the decreased amount of adhered unmelted Ti6Al4V metal particles to the surface, but undercovering the presence of undulations caused by solidified melt pools which act as stress concentrations and potential fatigue crack nucleation sites. The SLM Ti6Al4V HIP and SLM Ti6Al4V HIP + blasted samples started off having a very similar fatigue life at higher maximum applied stresses, which further indicate how a slight change in surface roughness impacts high cycle fatigue versus low cycle fatigue which is expected. For the wrought samples, polishing the machined sample yielded only modest improvement in surface finish (machined samples are 3x rougher than polished), yet had minimal impact on fatigue strength at runout to 1 million cycles (Fig. 8B). This suggests after a critical surface roughness of about 0.2 μm, further decreases in roughness are relatively ineffective in altering fatigue properties.

For the SLM Co28Cr6Mo samples (Fig. 8C), machining increases the fatigue life by 60 % whereas polishing the sample increases the fatigue life by 40 % (machining decreases the surface roughness by around 30x and polishing the surface decreases the surface roughness by ~27x). These effects are not as profound as those observed for SLM Ti6Al4V HIP samples (8 vs 5 μm). The difference in surface roughness is due to the visible melt pools which were not as prevalent on the surface of Co28Cr6Mo, so it may be expected to have less impact with subsequent surface processing. In addition, the results imply the Titanium alloy has better inherent fatigue resistance in the smooth state but is more sensitive to surface finish compared to the CoCr. The SLM Ti6Al4V HIP samples also had a different tensile behavior than the SLM Co28Cr6Mo samples due to the different material used.

With the EBM Ti6Al4V samples (Fig. 8D), polishing decreased the surface roughness by almost 160x but only increased the fatigue strength

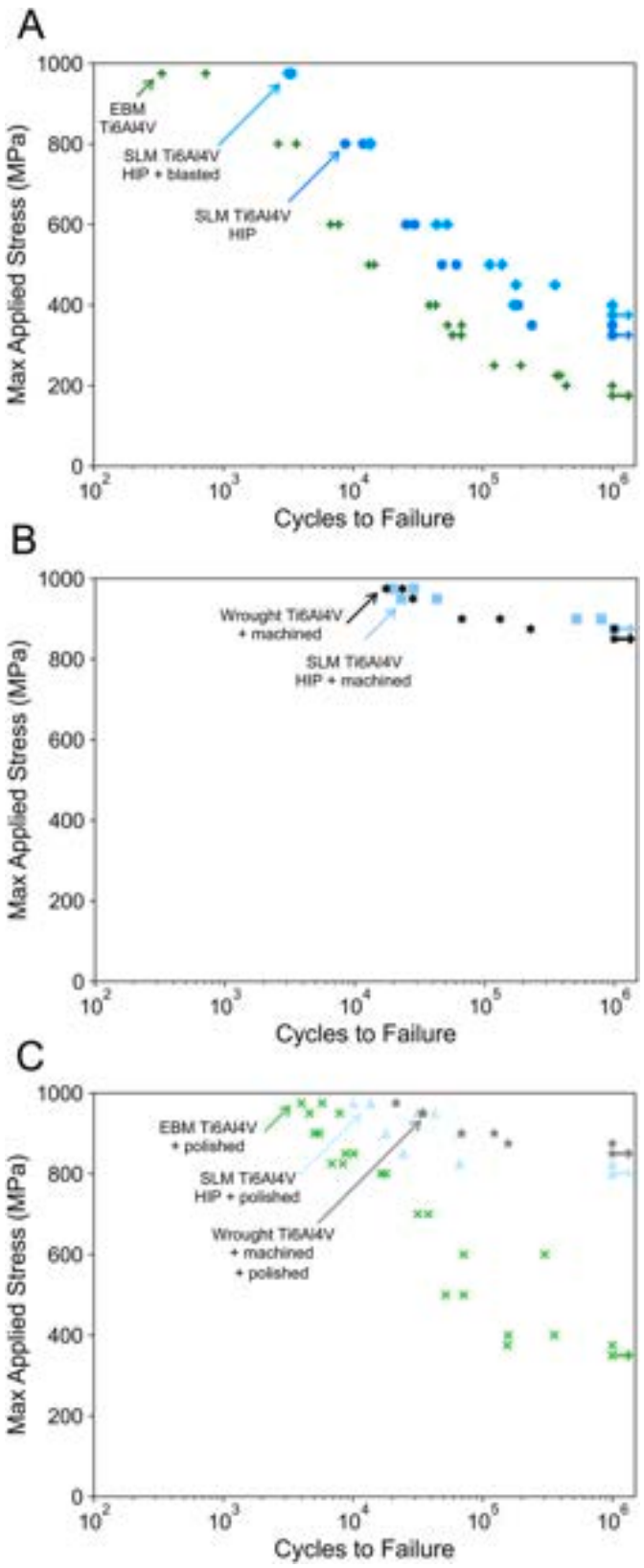

Fig. 9. Fatigue curves displaying the effect of manufacturing technique of A) as-printed and blasted variations B) machined variations and C) polished variations.

by 100 % compared to the 170 % increase in fatigue performance for a smaller roughness change in the SLM Ti6Al4V HIP materials. This data indicates that there is another factor aside from as-printed surface roughness impacting the fatigue life of the EBM Ti6Al4V samples, such as microstructure or larger internal defects from the process, the latter of which was observed in fractography.

For the porous gyroid samples (Fig. 8D), increasing the thickness of the added surface gyroid by 3x only decreases the fatigue strength by 12.5 %. The 0.50 mm surface gyroid had the lowest fatigue strength at 150 MPa. However, this fatigue strength is not much different than the fatigue strength of the 0.75 mm gyroid sample, since the 0.50 mm gyroid had one sample runout at 175 MPa with the other failing at 925k cycles. The SLM samples with the intentionally added 0.25 mm surface gyroid had a slightly better fatigue life than the as-printed EBM samples, which suggest that the SLM materials with added porosity have better fatigue properties than EBM without any porosity addition. All samples with gyroid surface structures had a lower fatigue strength than the solid SLM Ti6Al4V + HIP sample with a rough as-printed surface. This indicates that the stress concentration at the junction of gyroid wall and solid surface is greater than the stress concentration caused by inherent roughness of the SLM Ti6Al4V + HIP sample. The scale of the stress concentration in the surface roughness is also smaller than that of the gyroid porosity and the difference in fatigue behavior could also be a size/scale effect present in the fatigue of notched components.

3.4.2. *Process effect*

The effect of fabrication process (printing method or deformation processed wrought material) on fatigue life is conveyed in Fig. 9 where each Ti6Al4V sample is grouped based on mechanical post-processing method ("as-printed"/powder blasted, machined, and polishing). The SLM Ti6Al4V HIP + blasted samples were grouped with the "as-printed" as this post-processing didn't drastically alter the surface roughness (~8 vs 5 μm). In general, across the mechanical post-processing techniques, SLM Ti6Al4V HIP performed better than EBM Ti6Al4V, and SLM Ti6Al4V HIP performed similarly to the wrought Ti6Al4V samples.

SLM Ti6Al4V HIP'ed samples with an as-printed surface have a higher fatigue life than the EBM Ti6Al4V samples with an as-printed surface by more than 150 % (325 MPa max stress at runout vs 175 MPa). While EBM samples have a higher processing temperature that slows the cooling rate down to theoretically decrease the formation of α', the SLM samples received HIP'ing which also minimizes the size and number of internal defects from the PBF process while simultaneously altering the microstructure. Another difference in SLM and EBM samples with as-printed surfaces is the presence of much rougher surfaces in EBM samples which also drives down fatigue resistance.

The SLM Ti6Al4V HIP + machined samples had a similar fatigue life to the wrought Ti6Al4V samples (875 MPa max stress at runout vs 850 MPa). While these samples had differing microstructure, the similar fatigue life indicates that both morphologies of microstructure were strong and fatigue resistant and both contain minimal internal defects.

The wrought Ti6Al4V machined + polished samples perform slightly better than the SLM Ti6Al4V HIP + polished samples (850 MPa max applied stress at runout vs 800 MPa). The wrought Ti6Al4V samples went from machining straight to polishing whereas the SLM Ti6Al4V HIP + polished samples went from a rougher surface finish from 3D printing to polished (wrought samples had a starting roughness of ~0.2 μm whereas the SLM Ti6Al4V HIP + polished samples started with ~8 μm). While the SLM Ti6Al4V HIP + polished overall had a smoother surface, there were some macroscopic irregularities in the sample due to the hand polishing process. The microstructure of SLM and wrought were also different. However, due to only slight changes in fatigue life, this suggests that fatigue life was still dominated by defects (internal or external). The fatigue life of the EBM polished samples were significantly lower than both the polished SLM and polished wrought samples (approximately 40 % lower than SLM and wrought polished samples). While all three processing methods produce different microstructures

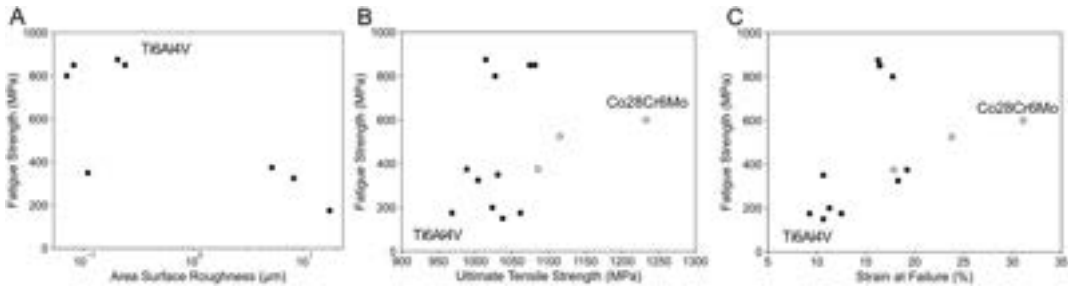

Fig. 10. Correlations between A) fatigue stress at runout vs surface roughness of only Ti6Al4V samples B) fatigue stress at runout vs tensile strength C) fatigue stress at runout vs strain at failure.

Table 2
Sample information for fracture analysis.

Sample Name	Applied Stress (MPa)	Cycles to Failure
SLM Ti6Al4V HIP	350	239,592
SLM Ti6Al4V HIP + blasted	450	361,084
SLM Ti6Al4V HIP + machined	900	793,992
SLM Ti6Al4V HIP + polished	825	66,367
EBM Ti6Al4V	200	441,324
EBM Ti6Al4V + polished	400	356,993
wrought Ti6Al4V + machined	875	226,668
wrought Ti6Al4V + machined + polished	875	156,950
SLM Co28Cr6Mo	400	622,406
SLM Co28Cr6Mo + machined	650	451,938
SLM Co28Cr6Mo + polished	550	771,522
SLM Ti6Al4V HIP + 0.25 mm gyroid	225	467,370
SLM Ti6Al4V HIP + 0.5 mm gyroid	175	925,580
SLM Ti6Al4V HIP + 0.75 mm gyroid	200	487,534

and slightly different surface finishes (the effect of which is minimized by polished), this suggests that the EBM process still does not have an optimized enough processing temperature to offset the HIP of SLM samples and the deformation processing and annealing of wrought samples for a better microstructure. Additionally due to the process, the larger particle size in EBM creates larger defects on the surface and internally.

3.5. Fatigue trends

While surface roughness exhibits an inverse correlation to the fatigue strength (the rougher the surface, the lower the fatigue strength) (Fig. 10A), at a certain point (below ~0.2 μm) the roughness effect starts to plateau in Fig. 10. The outlier in Fig. 10A is the EBM polished sample which while smooth, has other factors impeding the fatigue life such as sub surface internal defects brought to the surface and a different intrinsic microstructure. Fig. 10A highlights the inherently lower fatigue strength of the EBM material irrespective of surface finish. The best performing solid sample was the SLM Ti6Al4V HIP + machined sample (~0.2 μm surface roughness with a fatigue strength of 875 MPa). The worst performing sample was the as-printed EBM Ti6Al4V sample (~17 μm surface roughness and a fatigue strength of 175 MPa). With increasing the surface roughness 85x, the fatigue strength of a solid sample decreases 5 times. This is due to the surface roughness acting as micro notches and with decreasing surface roughness, the micro notches are decreased. Therefore, the stress concentration is decreased, and more force is required for the crack to initiate.

While each sample had varying tensile strengths, that factor did not correlate as strongly as surface finish, highlighting the importance of surface finish over tensile strength in predicting relative fatigue strength or printed metals. This may be due to the tensile curves amongst the various samples being relatively similar amongst the Ti6Al4V samples within the same processing group. There are two distinct separate groupings for the Ti6Al4V samples Fig. 10B, with the group with the higher fatigue stress being the machined and polished samples for the wrought and SLM Ti6Al4V. On the other hand, the strain at failure (also influenced by local stress concentrations similarly to fatigue) displays a positive correlation to the fatigue life (Fig. 10C) (as strain at failure increases so does fatigue life), except for smoother Ti6Al4V surfaces such as the machined and polished surfaces. This indicates that there are other factors besides ductility influencing fatigue resistance once the surface finish of a sample reaches a certain threshold (around 0.2 μm).

3.6. Fracture analysis

A table representing the samples for fracture analysis as well as the failure stress and cycles to failure is displaying in Table 2. Optical microscope images (Fig. 11) display one crack initiation point for the majority of the samples in the high cycle fatigue regime with the exception of the surface gyroid samples which appear to have multiple crack initiation sites with one primary one propagating and causing failure. SEM images (Fig. 12) display these initiation sites at the surface or sub surface of each specimen. The EBM Ti6Al4V samples display larger defects both at or just below the surface (approximately 100 μm in size) which seem to be lack of fusion defects. These defects have an irregular and asymmetrical shape that are detrimental in fatigue. On the fracture surface of the EBM Ti6Al4V + polished sample, a spherical pore (indicative of a gas pore) is also present. The SLM Ti6Al4V HIP and SLM Co28Cr6Mo samples also have internal defects (regardless of mechanical surface post-processing) but are much smaller than the EBM defects due to the smaller particle size during processing as well as the HIP post-processing treatment. The wrought Ti6Al4V samples appear to have the smallest crack initiation points (also having small surface area roughness measurements) and would also explain their very slightly enhanced performance in fatigue relative to the SLM printed titanium. These crack initiation points appear to be internal defects during the manufacturing process that are brought close to the surface during machining and polishing.

The gyroid samples had several cracks around the solid-porous interface (where gyroid walls meets solid surface) as well as where the corner of the gyroid meets the solid surface. The cracks starting around the interface could be due to the change in infill parameters during the printing process. It was expected for the cracks to initiate at the corner of the gyroid and solid surfaces, since that spot has a sharper angle for stress to concentrate. The SLM Ti6Al4V + 0.75 mm gyroid sample displayed two locations that caused failure.

4. Conclusion

This study investigated the effect of material (Ti6Al4V versus Co28Cr6Mo), manufacturing technique (EBM, SLM, Wrought), and surface finish (as printed, blasted, machined, polished, added surface porosity) on fatigue life of solid samples. These samples were all tested in tension-tension fatigue using identical testing parameters and sample geometry. These results can help optimize surface topographies multiple

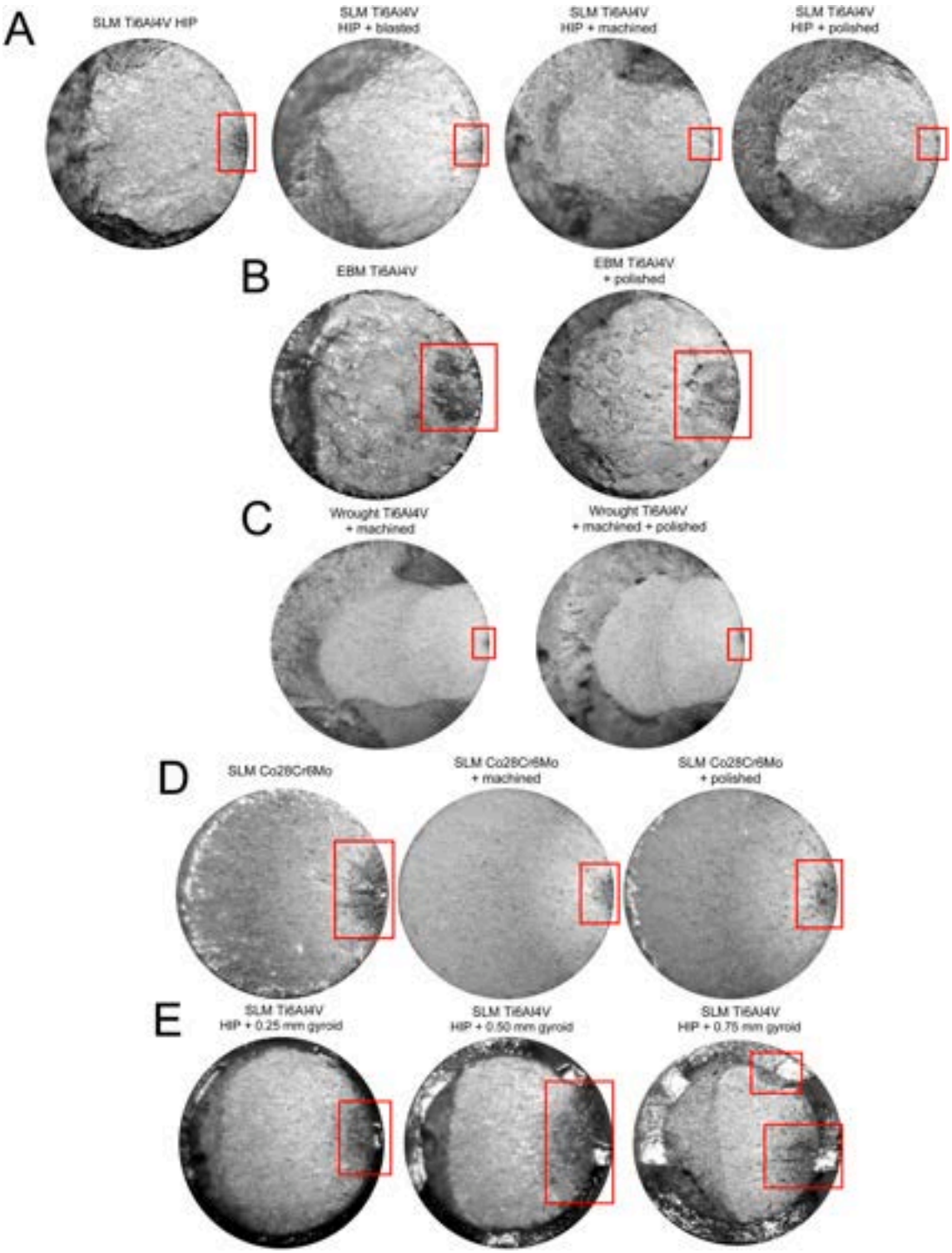

Fig. 11. Optical microscope images of fracture surfaces of representative A) SLM Ti6Al4V HIP variations (~5 mm in diameter) B) EBM Ti6Al4V variations (~5 mm in diameter) C) wrought Ti6Al4V variations (~5 mm in diameter) D) SLM Co28Cr6Mo variations (~5 mm in diameter) E) SLM Ti6Al4V HIP + gyroid variations (~5.6 mm in diameter for SLM Ti6Al4V HIP + 0.25 mm gyroid, ~6 mm in diameter for SLM Ti6Al4V HIP + 0.50 mm gyroid, and ~6.6 mm in diameter for SLM Ti6Al4V HIP + 0.75 mm gyroid).

applications.

The most prominent findings can be summarized as follows (also see Table 1):

5. Despite distinct microstructures with similar mechanical post-processing, SLM and wrought samples closely matched each other and outperformed EBM samples in fatigue due higher surface roughness and larger internal defects in EBM.
6. SLM Ti6Al4V HIP materials have an inherently higher fatigue resistance than SLM Co28Cr6Mo materials (fatigue properties in machined or polished states), but the Ti materials are relatively more

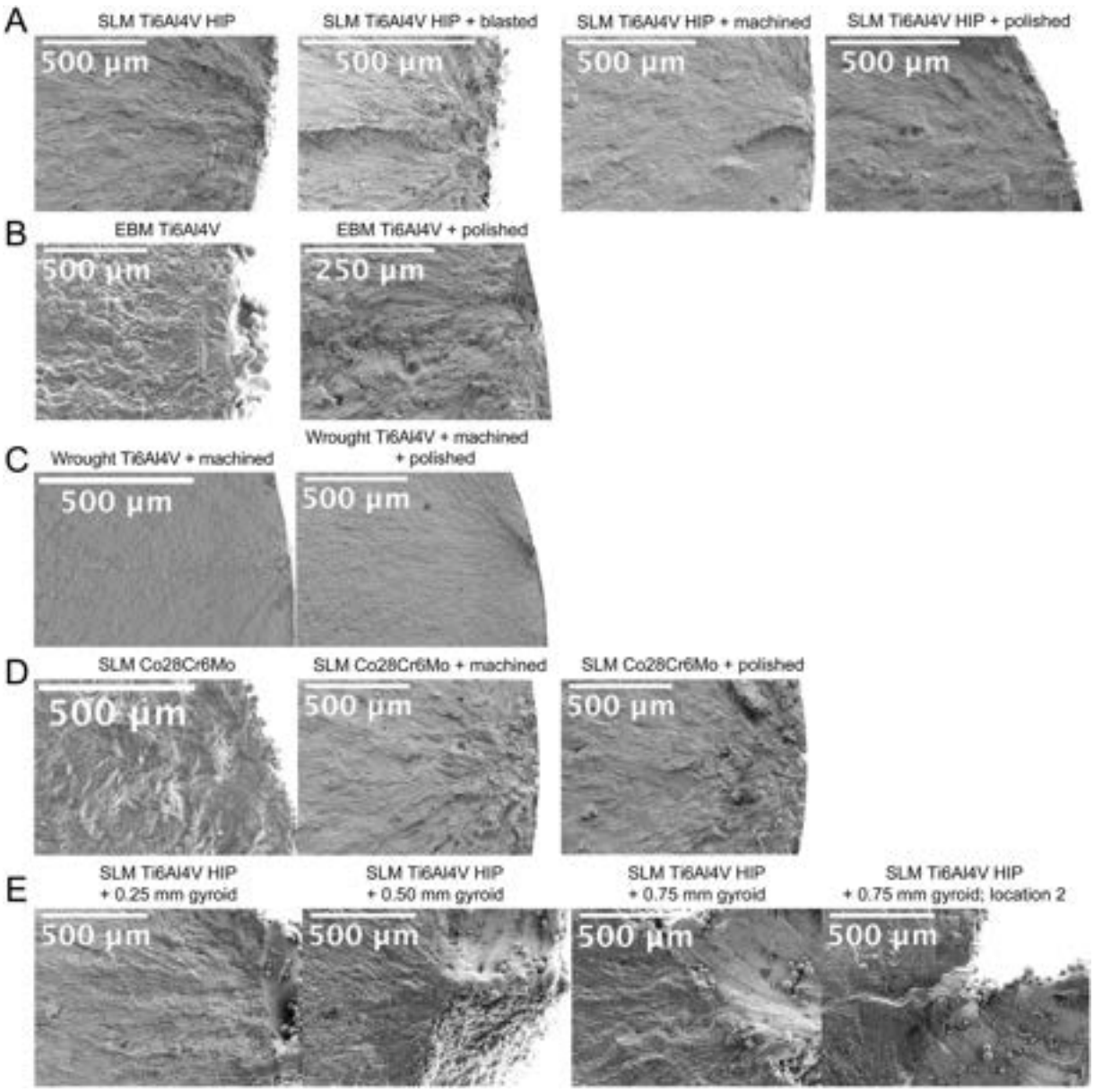

Fig. 12. SEM images of fracture surfaces of representative A) SLM Ti6Al4V HIP variations B) EBM Ti6Al4V variations C) wrought Ti6Al4V variations D) SLM Co28Cr6Mo variations E) SLM Ti6Al4V HIP + gyroid variations.

sensitive to the presence of surface roughness, seeing a larger drop in fatigue strength with the addition of a rough surface.

7. Mechanical post processing improved fatigue strength across all sample groups, but after a critical surface roughness of about 0.2 µm, further decreasing the surface roughness is relatively ineffective in increasing fatigue strength.
8. Adding 0.25 mm of porous gyroid to the surface of a SLM Ti6Al4V HIP sample yields a lower fatigue strength than rough as-printed SLM surfaces, but higher fatigue strength than the solid samples with the roughest as-printed surface (EBM Ti6Al4V). Increasing gyroid thickness had a limited additional impact on fatigue strength.
9. In HCF, samples failed from surface or sub surface defects with EBM samples displaying the largest surface and internal defects, including gas pores.

CRediT authorship contribution statement

Amanda Heimbrook: Writing – review & editing, Writing – original draft, Visualization, Validation, Investigation, Formal analysis, Data curation. **Ken Gall:** Writing – review & editing, Supervision, Resources, Project administration, Funding acquisition, Conceptualization.

Declaration of competing interest

The authors declare the following financial interests/personal relationships which may be considered as potential competing interests:

Ken Gall reports a relationship with restor3d that includes: board membership, employment, and equity or stocks. If there are other authors, they declare that they have no known competing financial interests or personal relationships that could have appeared to influence the work reported in this paper.

Data availability

Data will be made available on request.

Acknowledgement of funding sources

This work was performed in part at the Duke University Shared Materials Instrumentation Facility (SMIF), a member of the North Carolina Research Triangle Nanotechnology Network (RTNN), which is supported by the National Science Foundation (award number ECCS-2025064) as part of the National Nanotechnology Coordinated Infrastructure (NNCI).

Appendix A. Supplementary data

Supplementary data to this article can be found online at https://doi.org/10.1016/j.msea.2024.146821.

References

[1] L.M. Ricles, J.C. Coburn, M. Di Prima, S.S. Oh, "Regulating 3D-printed medical products," (in eng), Sci. Transl. Med. 10 (461) (Oct 3 2018), https://doi.org/10.1126/scitranslmed.aan6521.
[2] C.N. Kelly, et al., High-strength, porous additively manufactured implants with optimized mechanical osseointegration, Biomaterials 279 (2021/12/01/2021) 121206, https://doi.org/10.1016/j.biomaterials.2021.121206.
[3] K. Sathish, et al., A comparative study on subtractive manufacturing and additive manufacturing, Adv. Mater. Sci. Eng. 2022 (2022).
[4] M. Bowers, et al., Failure analysis of medical devices, J. Fail. Anal. Prev. 22 (1) (2022/02/01 2022) 154–180, https://doi.org/10.1007/s11668-021-01332-2.
[5] Q. Xin, 2 - durability and reliability in diesel engine system design, in: Q. Xin (Ed.), Diesel Engine System Design, Woodhead Publishing, 2013, pp. 113–202.
[6] H.D. Nguyen, et al., A critical review on additive manufacturing of Ti-6Al-4V alloy: microstructure and mechanical properties, J. Mater. Res. Technol. 18 (2022/05/01/2022) 4641–4661, https://doi.org/10.1016/j.jmrt.2022.04.055.
[7] D. Kumar, S. Idapalapati, W. Wang, S. Narasimalu, Effect of surface mechanical treatments on the microstructure-property-performance of engineering alloys, Materials 12 (16) (2019) 2503 [Online]. Available: https://www.mdpi.com/1996-1944/12/16/2503.
[8] J. Nafar Dastgerdi, O. Jaberi, H. Remes, Influence of internal and surface defects on the fatigue performance of additively manufactured stainless steel 316L, Int. J. Fatig. 163 (2022/10/01/2022) 107025, https://doi.org/10.1016/j.ijfatigue.2022.107025.
[9] S.M. Ahmadi, et al., Fatigue performance of additively manufactured meta-biomaterials: the effects of topology and material type, Acta Biomater. 65 (2018/01/01/2018) 292–304, https://doi.org/10.1016/j.actbio.2017.11.014.
[10] F. Cao, T. Zhang, M.A. Ryder, D.A. Lados, A review of the fatigue properties of additively manufactured Ti-6Al-4V, J. Occup. Med. 70 (3) (2018/03/01 2018) 349–357, https://doi.org/10.1007/s11837-017-2728-5.
[11] Ó. Teixeira, F.J.G. Silva, L.P. Ferreira, E. Atzeni, A review of heat treatments on improving the quality and residual stresses of the Ti–6Al–4V parts produced by additive manufacturing, Metals 10 (8) (2020) 1006 [Online]. Available: https://www.mdpi.com/2075-4701/10/8/1006.
[12] M. Kahlin, et al., Improved fatigue strength of additively manufactured Ti6Al4V by surface post processing, Int. J. Fatig. 134 (2020/05/01/2020) 105497, https://doi.org/10.1016/j.ijfatigue.2020.105497.
[13] B. Vayssette, N. Saintier, C. Brugger, M. El May, Surface roughness effect of SLM and EBM Ti-6Al-4V on multiaxial high cycle fatigue, Theor. Appl. Fract. Mech. 108 (2020/08/01/2020) 102581, https://doi.org/10.1016/j.tafmec.2020.102581.
[14] G. Szczęsny, M. Kopec, D.J. Politis, Z.L. Kowalewski, A. Łazarski, T. Szolc, A review on biomaterials for orthopaedic surgery and traumatology: from past to present (in eng), Materials 15 (10) (May 18 2022), https://doi.org/10.3390/ma15103622.
[15] L. Tonelli, M.M.Z. Ahmed, L. Ceschini, A novel heat treatment of the additively manufactured Co28Cr6Mo biomedical alloy and its effects on hardness, microstructure and sliding wear behavior, Progress in Additive Manufacturing 8 (2) (2023/04/01 2023) 313–329, https://doi.org/10.1007/s40964-022-00334-2.
[16] V. Bhavar, P. Kattire, V. Patil, S. Khot, K. Gujar, R. Singh, A review on powder bed fusion technology of metal additive manufacturing, Additive manufacturing handbook (2017) 251–253.
[17] A. Vafadar, F. Guzzomi, A. Rassau, K. Hayward, Advances in metal additive manufacturing: a review of common processes, industrial applications, and current challenges, Appl. Sci. 11 (3) (2021) 1213.
[18] T. Kurzynowski, M. Madeja, R. Dziedzic, K. Kobiela, The effect of EBM process parameters on porosity and microstructure of Ti-5Al-5Mo-5V-1Cr-1Fe alloy (in eng), Scanning 2019 (2019) 2903920, https://doi.org/10.1155/2019/2903920.
[19] H. Gong, K. Rafi, H. Gu, T. Starr, B. Stucker, Analysis of defect generation in Ti–6Al–4V parts made using powder bed fusion additive manufacturing processes, Addit. Manuf. 1–4 (2014/10/01/2014) 87–98, https://doi.org/10.1016/j.addma.2014.08.002.
[20] M. Kahlin, H. Ansell, J.J. Moverare, Fatigue behaviour of notched additive manufactured Ti6Al4V with as-built surfaces, Int. J. Fatig. 101 (2017/08/01/2017) 51–60, https://doi.org/10.1016/j.ijfatigue.2017.04.009.
[21] S. Liu, Y.C. Shin, Additive manufacturing of Ti6Al4V alloy: a review, Mater. Des. 164 (2019/02/15/2019) 107552, https://doi.org/10.1016/j.matdes.2018.107552.
[22] A.B. Novaes Jr., S.L. S.d. Souza, R.R. M.d. Barros, K.K.Y. Pereira, G. Iezzi, A. Piattelli, Influence of implant surfaces on osseointegration, Braz. Dent. J. 21 (2010).
[23] I.S. Grech, J.H. Sullivan, R.J. Lancaster, J. Plummer, N.P. Lavery, The optimisation of hot isostatic pressing treatments for enhanced mechanical and corrosion performance of stainless steel 316L produced by laser powder bed fusion, Addit. Manuf. 58 (2022) 103072, https://doi.org/10.1016/j.addma.2022.103072, 2022/10/01/.
[24] B. Fotovvati, N. Namdari, A. Dehghanghadikolaei, Fatigue performance of selective laser melted Ti6Al4V components: state of the art, Mater. Res. Express 6 (1) (2018) 012002.
[25] C. Liu, et al., Effect of hot isostatic pressing on microstructures and mechanical properties of Ti6Al4V fabricated by electron beam melting, Metals 10 (5) (2020) 593.
[26] N. Razavi, A. Avanzini, G. Cornacchia, L. Giorleo, F. Berto, Effect of heat treatment on fatigue behavior of as-built notched Co-Cr-Mo parts produced by Selective Laser Melting, Int. J. Fatig. 142 (2021) 105926, https://doi.org/10.1016/j.ijfatigue.2020.105926, 2021/01/01/.
[27] J.E. LaRue, S.R. Daniewicz, Predicting the effect of residual stress on fatigue crack growth, Int. J. Fatig. 29 (3) (2007/03/01/2007) 508–515, https://doi.org/10.1016/j.ijfatigue.2006.05.008.
[28] B. Vayssette, N. Saintier, C. Brugger, M. Elmay, E. Pessard, Surface roughness of Ti-6Al-4V parts obtained by SLM and EBM: effect on the high cycle fatigue life, Procedia Eng. 213 (2018/01/01/2018) 89–97, https://doi.org/10.1016/j.proeng.2018.02.010.
[29] A. Fatemi, et al., Fatigue behaviour of additive manufactured materials: an overview of some recent experimental studies on Ti-6Al-4V considering various processing and loading direction effects, Fatig. Fract. Eng. Mater. Struct. 42 (5) (2019) 991–1009, https://doi.org/10.1111/ffe.13000.
[30] K. Moussaoui, M. Mousseigne, J. Senatore, R. Chieragatti, P. Lamesle, Influence of milling on the fatigue lifetime of a Ti6Al4V titanium alloy, Metals 5 (3) (2015) 1148–1162.
[31] L. Koroleva, Final polishing of metals to obtain nanoroughened surface, Nanotechnologies in Russia 7 (1) (2012) 67–75.
[32] P. Tyagi, T. Goulet, C. Riso, F. Garcia-Moreno, Reducing surface roughness by chemical polishing of additively manufactured 3D printed 316 stainless steel components, Int. J. Adv. Des. Manuf. Technol. 100 (9) (2019/02/01 2019) 2895–2900, https://doi.org/10.1007/s00170-018-2890-0.
[33] S. Chang, et al., Highly effective smoothening of 3D-printed metal structures via overpotential electrochemical polishing, Materials Research Letters 7 (7) (2019/07/03 2019) 282–289, https://doi.org/10.1080/21663831.2019.1601645.
[34] A. Krishnan, F. Fang, Review on mechanism and process of surface polishing using lasers, Front. Mech. Eng. 14 (3) (2019/09/01 2019) 299–319, https://doi.org/10.1007/s11465-019-0535-0.
[35] L. Liu, Z. Zhang, B. Wu, W. Hu, F. Meng, Y. Li, A review: green chemical mechanical polishing for metals and brittle wafers, J. Phys. Appl. Phys. 54 (2021) 373001.
[36] P. Li, D.H. Warner, A. Fatemi, N. Phan, Critical assessment of the fatigue performance of additively manufactured Ti–6Al–4V and perspective for future research, Int. J. Fatig. 85 (2016/04/01/2016) 130–143, https://doi.org/10.1016/j.ijfatigue.2015.12.003.
[37] P. Jamshidi, et al., Selective laser melting of Ti-6Al-4V: the impact of post-processing on the tensile, fatigue and biological properties for medical implant applications, Materials 13 (12) (2020) 2813 [Online]. Available: https://www.mdpi.com/1996-1944/13/12/2813.
[38] C.N. Kelly, et al., Fatigue behavior of As-built selective laser melted titanium scaffolds with sheet-based gyroid microarchitecture for bone tissue engineering, Acta Biomater. 94 (2019/08/01/2019) 610–626, https://doi.org/10.1016/j.actbio.2019.05.046.
[39] S. Acharya, R. Soni, S. Suwas, K. Chatterjee, Additive manufacturing of Co–Cr alloys for biomedical applications: a concise review, J. Mater. Res. 36 (19) (2021/10/01 2021) 3746–3760, https://doi.org/10.1557/s43578-021-00244-z.
[40] M. Roudnicka, J. Bigas, V. Sreibr, D. Palousek, D. Vojtech, Direct comparison between Co-28Cr-6Mo alloy prepared by Selective Laser Melting and traditional investment casting, IOP Conf. Ser. Mater. Sci. Eng. 1178 (1) (2021/08/01 2021) 012046, https://doi.org/10.1088/1757-899X/1178/1/012046.
[41] E. Salsi, M. Chiumenti, M. Cervera, Modeling of microstructure evolution of Ti6Al4V for additive manufacturing, Metals 8 (8) (2018) 633 [Online]. Available: https://www.mdpi.com/2075-4701/8/8/633.
[42] A. Fatemi, R. Molaei, N. Phan, Multiaxial fatigue of additive manufactured metals, MATEC Web Conf. 300 (2019) 01003, https://doi.org/10.1051/matecconf/201930001003 [Online]. Available:.
[43] J. Xi, et al., The low-cycle fatigue behavior, failure mechanism and prediction of SLM Ti-6Al-4V alloy with different heat treatment methods, Materials 14 (21) (2021) 6276 [Online]. Available: https://www.mdpi.com/1996-1944/14/21/6276.
[44] H.K. Rafi, N.V. Karthik, H. Gong, T.L. Starr, B.E. Stucker, Microstructures and mechanical properties of Ti6Al4V parts fabricated by selective laser melting and electron beam melting, J. Mater. Eng. Perform. 22 (12) (2013/12/01 2013) 3872–3883, https://doi.org/10.1007/s11665-013-0658-0.
[45] T. Pasang, et al., Directionally-dependent mechanical properties of Ti6Al4V manufactured by electron beam melting (EBM) and selective laser melting (SLM) (in eng), Materials 14 (13) (Jun 28 2021), https://doi.org/10.3390/ma14133603.

[46] T.M. Mower, M.J. Long, Mechanical behavior of additive manufactured, powder-bed laser-fused materials, Mater. Sci. Eng., A 651 (2016/01/10/2016) 198–213, https://doi.org/10.1016/j.msea.2015.10.068.
[47] B. Konieczny, A. Szczesio-Wlodarczyk, J. Sokolowski, K. Bociong, Challenges of Co–Cr alloy additive manufacturing methods in dentistry—the current state of knowledge (systematic review), Materials 13 (16) (2020) 3524 [Online]. Available: https://www.mdpi.com/1996-1944/13/16/3524.
[48] Y. Kajima, et al., Effect of heat-treatment temperature on microstructures and mechanical properties of Co–Cr–Mo alloys fabricated by selective laser melting, Mater. Sci. Eng., A 726 (2018/05/30/2018) 21–31, https://doi.org/10.1016/j.msea.2018.04.048.